Band Gap Regulation Mechanism and Rule of Locally Resonant Thermo-Magneto-Mechanical Phononic Crystal Double-Layer Nanobeam Based on Symmetric and Antisymmetric Vibration Modes

Litao Zhou, Long Ren, Qi Wang, Tianao Wang, Daojie Jiang, Dongdong Wang and Chenghao Zhao

China Nanhu Academy of Electronics and Information Technology, Jiaxing, China, 314000.

Denghui Qian

School of Naval Architecture & Ocean Engineering, Jiangsu University of Science and Technology, Zhenjiang 212100, Jiangsu, China. E-mail: dhqian@just.edu.cn

(Received 4 January 2025; accepted 23 February 2025)

A locally resonant (LR) thermo-magneto-mechanical (TMM) phononic crystal (PC) double-layer nanobeam is presented, which is achieved by periodically attaching "vertical spring-precompressed horizontal spring-additional spring-mass" resonators onto the surface of lower and upper nanobeams. The band structure is calculated with surface elastic theory and TMM coupling constitutive Euler beam model, which are applied to the plane wave expansion (PWE) method. Three unabridged band gaps can be effectively exposed under 10 GHz. Vibration modal analysis improves that all the bands can be divided into symmetry bands and antisymmetry bands. Precompressed horizontal springs and extra springs can aid in further widening band gaps based on such a creation mechanism. Besides, with the growth of stiffness of horizontal and additional springs, the widths of band gaps increase. The unique symmetric and antisymmetric regulation mechanism and rule of double-layer nanobeam is unpossessed of single-layer nanobeam. It is envisaged that all of these studies will be applied to active vibration control in nano TMM systems.

1. INTRODUCTION

With the speedy development of new materials, various nano systems based on the multi-physics interface between thermotics, magnetism, and mechanics have attracted great attention with their obvious features such as ultra-high frequency, high sensitivity, low energy consumption, small size, etc. They can be used in the fields of biomedicine, social affairs, national defense, and so on.[1] Because of most TMM nanodevices being constructed by some basic structures like beam and plate, research on the thermo-magneto-mechanical nanostructures is meaningful. With the existence of band gaps, PC, a type of artificial periodic composite structure, has been extensively studied and applied in acoustical devices, acoustic lenses, vibration and noise control, and other applications.[2] Hence, the design thought of PC can be applied to TMM nanodevice to[2] form TMM PC nanostructure with the common application prospect in vibrational and acoustical devices. With the coupling of PC, nanomaterial and TMM material, both exceptional performances and novel physical attributes will be showcased. Besides, A wide range of applications for TMM nano systems will be opened by further research into TMM PC nanostructures.

Recently, limited direct studies on TMM PC nanostructures have been conducted. By introducing surface impact[1] and nonlocal effects[3] into the PWE method, the influences of surface effects, nonlocal effects, prestress, magnetic field and geometric parameters on band structures were investigated by Zhang and Hu et al. A TMM PC nanobeam was proposed by regularly combining the magnetostrictive material Terfenol-D with the elastic material epoxy. Qian et al. investigated the effects of geometrical parameters, surface effects, as well as thermo-magneto-mechanical forces on the band gap.[4] Additionally, the LR TMM PC single-layer nanobeam was proposed by regularly attaching "spring-mass" resonators on magnetostrictive material Terfenol-D. The influence law of the resonator, thermo-magneto-mechanical fields, surface effects, and geometric factors on band gaps were considered. Besides, a singular pre-stress was present to make the band gaps not be opened easily, and the influencing rules of parameters on singular prestress was discussed by Qian et al.[5] Ding et al.[6] have theoretically investigated the control and regulation of the longitudinal band structure of one-dimensional rod-like phononic crystals of magnetostrictive materials using the plane wave expansion method. A quasistatic hysteresis model revealing the hysteresis behavior of Terfenol-D was developed by Zhang et al.[7] It can be concluded that a wider research space on TMM PC nanostructures still existed.

In general, the mechanical properties depending on the type

of TMM nanostructures and the band gap properties of different PCs were investigated. It has been demonstrated both theoretically and experimentally that nanostructures are not subject to the size-dependent nature of traditional continuum elastic theory. Nonetheless, by making corrections to the classical continuum elasticity theory, certain higher-order continuum elasticity theories, such as nonlocal,[3,9,10] surface,[1,11] strain gradient,[12] and couple stress,[13] have been presented. Surface elasticity theory[14] has been used to further improve surface TMM theory, which aims to optimize the TMMc nanostructures. In the field of PC over the last three decades, various methods and related studies focusing on the macro scale have been carried out. Therefore, many PC bars, beams, plates, etc.[15,16] It has been developed and is being worked on to meet technical requirements. Some multi-physics coupling PC constructions, such as magneto-electro-elastic, piezomagnetic, and piezoelectric PCs,[17–19] emerge to overcome the uncontrollability of band gap. Among these, the TMM PCs' mechanical, magnetic, and thermal properties may all be altered to accurately control the band gaps. The ultrahigh vibrational control can be achieved if the PC structure's size is lowered to the nanoscale since this will significantly raise the magnitude order to gigahertz (GHz) and even from hertz (Hz) to terahertz (THz).[20,21]

It is well known, the frequency range of vibration control is constant if the structure is certain. Hence, the introduction of magnetostrictive material can realize the dynamic vibration control with the interconversion between magnetic and mechanical fields. Besides, adding resonant units can be more efficient to widen frequency range. Based on the previous researches on magneto-elastic and piezoelectric PC nanobeams with surface and nonlocal effects, the physical and computational models of a magnetostrictive LR PC nanobeam with the consideration of multi-physics coupling of thermotics, magnetics and mechanics is proposed in this paper. Euler beam and surface TMM theories are combined into the PWE approach based on the research on TMM nanostructures and PCs. In order to demonstrate the unmatched tunability, the band structures of the suggested LR TMM PC double-layer nanobeams are computed and acquired, and the formation mechanisms and influence rules are investigated.

2. MODEL AND METHOD

Figure 1 shows that the model of LR TMM PC double-layer nanobeam consisted of two components: middle layer resonator and upper (or lower) layer base nanobeam. Two different materials were picked to form the base nanobeam, which are magnetostrictive material Terfenol-D (rendered by gray) and elastic material epoxy (rendered by yellow), respectively. At the nanoscale, the two materials mentioned above repeat periodically along the x direction to form the base nanobeam. The resonator was composed by foundation, mass m_R, horizontal spring k_y, vertical spring k_z and additional spring k_A. In a unit cell, two horizontal springs were attached between mass and foundation, two vertical springs were attached between mass and double-layer nanobeam, one additional spring

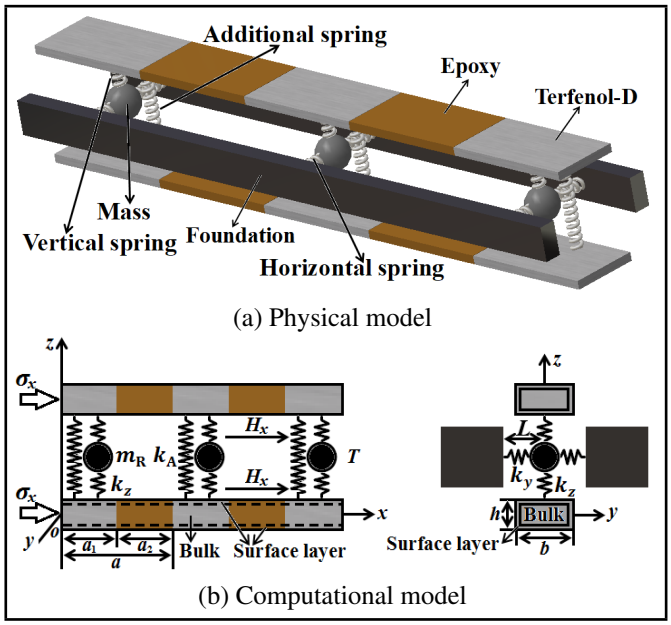

Figure 1. A LR TMM PC double-layer nanobeam model.

was attached between upper and lower layer nanobeams. Here, the midpoint of Terfenol-D in a unit cell was chosen as the attached point. All the horizontal springs with original length L_y were presupposed in y-direction if not vibrated. Length between mass and foundation is L and presuppose that horizontal springs are pre-compressed initially, that was $L < L_y$. As displayed in Fig. 1 (b), σ_x was the pre-stress in x-direction, H_x was the magnetic field in x-direction, T represented the operating temperature. The lattice constant of PC nanobeam was $a = a_1 + a_2$, where a_1 was the length of Terfenol-D and a_2 was the length of epoxy in a unit cell. The nanobeam was chosen as rectangular cross section with width b and thickness h. The location of resonator can be expressed as: $X = a_1/2 + \bar{m}a$, where $\bar{m} = 0, \pm1, \pm2, \ldots$. According to surface TMM theory,[14] the bulk core and surface layer were the two components that make up a nanobeam. Tables 1 and 2 give the material parameters of Terfenol-D and epoxy in bulk core. Among them, epoxy's Young's modulus E was related to T and the corresponding experimental data is shown in Table 2. In Table 1, ρ (Terfenol-D ρ_1 and epoxy ρ_2) was the density, the saturation magnetization was denoted by M_s, the linear magnetic susceptibility is denoted by χ_m, the saturated Young's modulus was represented by E_s, the vacuum permeability is represented by $\mu_0 = 4\pi \times 10^{-7} Hm^{-1}$, the saturated magnetostrictive stress was represented by σ_s, and the Curie temperature is indicated by T_c, severally.

Similar to LR TMM PC single-layer nanobeam,[5] the flexural vibration equations of double-layer nanobeam considering surface effects are as on the top of the next page.

In those equations, $W_l(X)$ was the displacement of lower-layer nanobeam in z-direction, $W_u(X)$ was the displacement of upper-layer nanobeam in z-direction, and $W_R(X)$ was the displacement of mass in z-direction at location X. $Q_l(X)$ was the resultant force applied to lower-layer nanobeam by vertical and additional springs, the resultant force applied by vertical and additional springs to the upper-layer nanobeam was de-

Table 1. Bulk material parameters of Terfenol-D and epoxy.[5]

Material	ρ/kgm^{-3}	χ_m	E_s/GPa	$\beta/\times 10^{-6}\circ C$	λ_s/ppm	$\mu_0 M_s/T$	σ_s/MPa	$T_c/^{circ}C$
Terfenol-D	9210	80	110	2.5	1300	0.8	200	383.3
epoxy	1180							

$$\begin{cases} \frac{\delta^2}{\delta x^2}\left(m(x)\frac{\delta^2 W_l(x)}{\delta x^2}\right) - n(x)\frac{\delta^2 W_l(x)}{\delta x^2} - \omega^2 o(x) W_u(x) = \sum_x Q_1(X) \\ -\omega^2 m_R W_R(X) = Q_R(X) \\ \frac{\delta^2}{\delta x^2}\left(m(x)\frac{\delta^2 W_u(x)}{\delta x^2}\right) - n(x)\frac{\delta^2 W_u(x)}{\delta x^2} - \omega^2 o(x) W_l(x) = \sum_x Q_1(X) \end{cases} \tag{1}$$

where:

$$\begin{cases} Q_l(X) = -k_z\left[W_l(X) - W_R(X)\right]\delta(x-X) - k_A\left[W_l(X) - W_u(X)\right]\delta(x-X) \\ Q_R(X) = k_z\left[W_l(X) - 2W_R(X) + W_u(X)\right] + 2k_Y\left[\frac{L_Y}{\sqrt{W_R^2(X)+L^2}} - 1\right]W_R(X) \\ Q_u(X) = -k_z\left[W_u(X) - W_R(X)\right]\delta(x-X) - k_A\left[W_u(X) - W_l(X)\right]\delta(x-X) \end{cases}; \tag{2}$$

Table 2. Young's modulus of epoxy at different operating temperatures.[20]

$T/^{circ}C$	-60	0	23	40	60	80	110
E/GPa	4621.24	3411.62	2701.42	2360.71	109.05	63.920	38.070

noted as $Q_u(X)$, while the resultant force applied by vertical and horizontal springs to the mass was denoted as $Q_R(X)$.The vibration circular frequency was represented by ω, while the one-dimensional (1D) delta function is shown by $\delta(x-X)$.

Besides, the self-difined parameters m_1, m_2, n_1, n_2, and o_1, o_2 were consistently denoted by the symbols $m(x)$, $n(x)$, and $0(x)$, where subscripts 1 and 2 express Terfenol-D and epoxy, respectively. Here are the specifics:

$$m_1(x) = \frac{bh^3}{12}\bar{c} + (\frac{bh^2}{2} + \frac{h^3}{6})\bar{c^s}; \tag{3}$$

$$n_1(x) = 2b(\sigma_x^0 - \frac{q_1 1^s \mu_0}{\mu_{11}}H_x) - \frac{bhq_{11}\mu_0}{\mu_{11}}H_x; \tag{4}$$

$$o_1 = \rho_1 bh; \tag{5}$$

$$m_2(x) = \frac{bh^3}{12}E + (\frac{bh^2}{2} + \frac{h^3}{6})E^s; \tag{6}$$

$$n_2(x) = 2b\sigma_x^0; \tag{7}$$

$$o_2 = \rho_2 bh; \tag{8}$$

where $\bar{c} = c_{11} + q_{11}^2/\mu_{11}$, $\bar{c^s} = c_{11}^s + q_{11}^s q_{11}/\mu_{11}$. c_{11} was the elastic coefficient, q_{11} was the piezomagnetic coefficient and μ_{11} was the magnetic permeability. The detail solution procedure of parameters c_{11}, q_{11} and μ_{11} can be seen in APPENDIX A. Based on surface TMM theory,[12] some new parameters according to surface effects are introduced. σ_x^0 was the residual surface stress, $\bar{c^s}$ was the surface elastic coefficient and q_{11}^s is the surface piezomagnetic coefficient. E^s is the surface Young's modulus of epoxy. Here, those bulk parameters are connected to all of the surface parameters:[12]

$$p_s \leftrightarrow l_s p_b; \tag{9}$$

where p_S and p_b uniformly denoted the relevant surface and bulk parameters, separately.

In addition, l_s represents the material intrinsic length.

If the second item of $Q_R(X)$ in Eq. (2) is expanded by Fourier series with second and higher order terms ignored, it can be linearized:

$$Q_R(X) = k_z[W(X) - W_R(X)] + 2k_y(l-1)W_R(X); \tag{10}$$

where $l = L_y/L$.

According to the periodicity along x-direction and 1D PWE method, Eq. (1) can be expanded to spatial Fourier series and matriculated[5,7] (see on the top of the next page), where

$$[MG]_{ij} = (k+G_i)^2 m(G_i i G_j)(k+G_j)^2; \tag{12}$$

$$[NG]_{ij} = n(G_i - G_j)(k+G_j)^2; \tag{13}$$

$$[OG]_{ij} = o(G_i - G_j); \tag{14}$$

$$[PG] = [1\,1\,\ldots\,1]_{1\times N}; \tag{15}$$

$$[QG] = [PG]^T[PG]; \tag{16}$$

$$\begin{cases} [W_l(G)] = [W_l(G_1)\,W_l(G_2)\,\ldots\,W_l(G_N)]^T \\ [W_u(G)] = [W_u(G_1)\,W_u(G_2)\,\ldots\,W_u(G_N)]^T \end{cases}; \tag{17}$$

Here, N was the number of interceptive reciprocal-lattice vector, G_i or G_j $(i,j = 1,2,3\ldots,N)$ was the ith or jth reciprocal-lattice vector, the Bloch wave vector confined to the irreducible first Brillouin zone (1BZ) is denoted by k, and $\xi(G_i - G_j)(\xi = m,n,o)$ is expressed as:

$$\xi(G_i - G_j) = \begin{cases} \xi_1 f + \xi_2(1-f)G_i - G_j = 0 \\ (\xi_1 - \xi_2)\psi(G_i - G_j)G_i - G_j \neq 0 \end{cases}; \tag{18}$$

where $f = a_1/a$ denoted the filling ratio of Terfenol-D, and $\psi(G_i - G_j) = f\sin[(G_i - G_j)a_1/2]/[(G_i - G_j)a_1/2]$.

One way to think of Eq. (11) is as a generalized eigenvalue equation typical. For each k, a series of eigenvalues ω^2 and corresponding eigenvectors $\begin{bmatrix}[W_l(G)] \\ W_R(0) \\ [W_u(G)]\end{bmatrix}$ can be obtained. Taking the Bloch wave vector k as the x-axis, the vibrational frequency $f = \omega/2\pi$ as the y-axis, the band structure can be

$$\left(\begin{bmatrix} a[MG]+a[NG]+k_z[QG]+k_A[QG] & -k_z[PG]^T & -k_A[QG] \\ -k_z[PG] & 2k_z-2k_y(l-1) & -k_z[PG] \\ -k_A[QG] & -k_z[PG]^T & a[MG]+a[NG]+k_z[QG]+k_A[QG] \end{bmatrix} - \omega^2 \begin{bmatrix} a[OG] & [0] & [0] \\ [0] & m_R & [0] \\ [0] & [0] & a[OG] \end{bmatrix} \right) \times \begin{bmatrix} [W_l(G)] \\ W_R(0) \\ [W_u(G)] \end{bmatrix} = [0]; \tag{11}$$

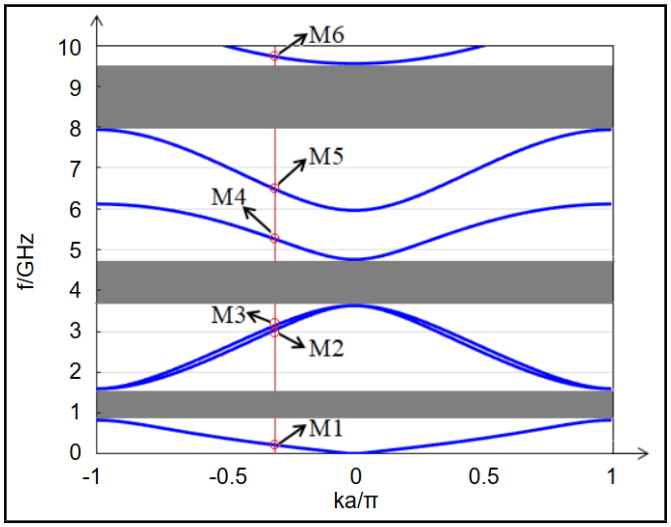

Figure 2. Band structure of LR TMM PC double-layer nanobeam without horizontal and additional springs.

drawn. For the given k and ω^2, the double-layer nanobeam's vibration mode is represented by the symbol:[9]

$$\begin{cases} W_l(x) = \sum_G W_l(G) e^{i(k_g)x} \\ W_u(x) = \sum_G W_u(G) e^{i(k_g)x} \end{cases} . \tag{19}$$

3. NUMERICAL RESULTS AND ANALYSES

3.1. Bands of LR TMM PC Double-Layer Nanobeam Vibrated in Symmetric and Antisymmetric Modes

Equation (11) is used to compute the band structure of the proposed LR TMM PC double-layer nanobeam, which is displayed in Fig. 2. Here, horizontal and additional springs are ignored, that is $k_y = 0$ N/m and $k_A = 0$ N/m. Besides, $T = 23°C$ and $E = 2701.42$ MPa by referring Table 2. Other parameters were set as: $\sigma_x = -20$ MPa, $H_x = 1$ kOe, $\sigma_x^0 = 1$ N/m^{-1}, $l_s = 1$ nm, $m_R = 1 \times 10^{-18}$ kg, $k_z = 1 \times 10^2$ N/m, $l = 2$, $a_1 = a_2 = 50$ nm and $b = h = 10$ nm. As demonstrated, three full band gaps with a total width of 3.5 GHz and an opening rate of $\eta = 35$ % were opened beneath 10 GHz. Among them, the first band gap was from 0.83 GHz to 1.59 GHz, between 3.63 GHz and 4.76 GHz was the second band gap, while between 7.94 GHz and 9.55 GHz was the third band gap, respectively. The vibration modes of M1, M2, M3, M4, M5, and M6 marked in Fig. 2 are derived using Eq. (19)in order to comprehend the production mechanism of band gaps.

Figure 3 gives the vibration modes of M1, M2, M3, M4, M5 and M6 in a unit cell. Two different colors gray and yellow are applied to express the magnetostrictive material Terfenol-D and elastic material epoxy, respectively. Two different mate-

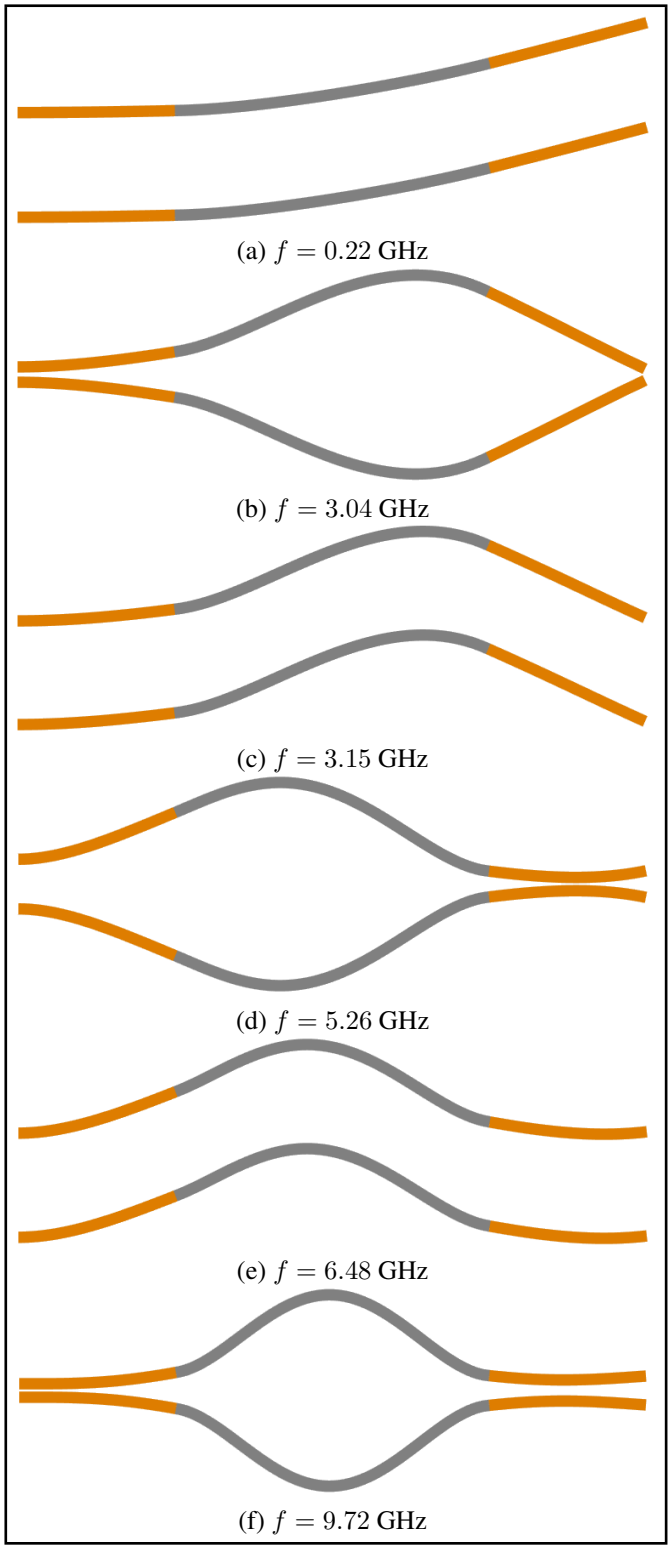

Figure 3. Vibration modes of M1, M2, M3, M4, M5 and M6.

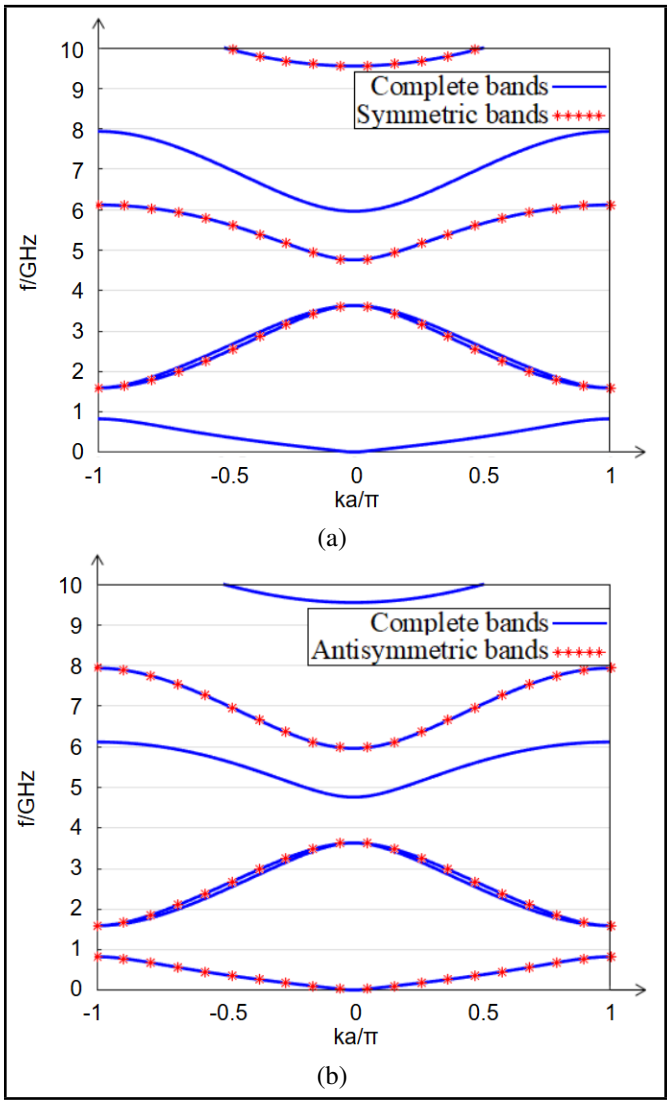

Figure 4. (a) Symmetric and (b) antisymmetric band structures of LR TMM PC double-layer nanobeam with horizontal and additional springs not attached.

rials are picked to form the base nanobeam, which are magnetostrictive material Terfenol-D (rendered by gray) and elastic material epoxy (rendered by yellow), respectively.

The vibration frequencies of M1, M2, M3, M4, M5 and M6 are 0.22 GHz, 3.04 GHz, 3.15 GHz, 5.26 GHz, 6.48 GHz and 9.72 GHz, respectively, which the located bands of M1, M2, M3, M4, M5 and M6 can be regarded as first, second, third, fourth, fifth and sixth order bands, separately. As shown, the first, third and fifth order bands are vibrated in antisymmetric modes as well as the second, fourth and sixth order bands are vibrated in symmetric modes.

To further reveal the symmetry and antisymmetry of bands, the additional constraint conditions are introduced to Eq. (1).

$W_l(x) = -W_u(x)$ and $W_R(X) = 0$ if the double-layer nanobeam vibrates in symmetric mode. After that, Eq. (11) can be simplified to:

$$(a[MG] + a[NG] + k_z[QG] + 2k_A[QG] - \\ - \omega^2 a[OG]) \times [W_l(G)] = [0]; \quad (20)$$

$W_l(x) = W_u(x)$ if the double-layer nanobeam vibrates in the antisymmetric mode.

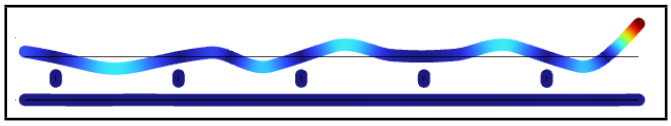

Figure 5. Vibration mode of LR TMM double-layer nanobeam with five periodicities in f=3 GHz.

Eq. (11) can therefore be simplified to (see the top of the next page.)

The band structures of the LR TMM PC double-layer nanobeam without additional springs vibrating in symmetric and antisymmetric modes are shown in Figs. 4 (a) and (b). Also included is the original band structure. As shown, the first, third and fifth order bands can be regarded as the antisymmetric bands as well as the second, fourth and sixth order bands can be regarded as the symmetric bands, which matches well with Fig. 3. If the bands are vibrated in symmetric mode, mass keeps still, which makes the symmetric bands unaffected by changing mass and horizontal spring k_y. However, the antisymmetric bands are affected by changing k_y. The antisymmetric bands are unaffected by the addition of spring k_A since, in this type of vibration mode, the spacing between the upper and lower layer nanobeams remains constant. However, the symmetric bands are influenced. Hence, the band structure and corresponding band gaps can be adjusted by adding horizontal and additional springs.

With the help of finite element software COMSOL, the vibration mode of LR TMM double-layer nanobeam with five periodicities can be obtained, as shown in Fig. 5. With the deepening of color, the amplitude of vibration is getting larger. Here, the excitation point is picked at the left point of upper-layer nanobeam and the corresponding frequency is $f = 3$ GHz. As shown, vibration can be easily propagated along the upper-layer nanobeam, but which can be effectively restrained along the lower-layer nanobeam. By reviewing Fig. 2 and Fig. 3, the actual vibration of double-layer nanobeam is the superposition of M2 and M3 if $f = 3$ GHz, which the vibration of upper-layer nanobeam is strengthened and the vibration of lower-layer nanobeam is counteracted on account of the symmetry and antisymmetry. Hence, if the excitation and response areas are located at different sides of double-layer nanobeam, the actual band gaps can be further opened, but not only shown as Fig. 2.

3.2. Influences of Additional and Horizontal Springs on Band Structures

The band structure of the LR TMM PC double-layer nanobeam with extra springs k_A attached is shown in Fig. 6 (a). As a contrast, the band structure of the nanobeam is similarly shown in 6 (a), but without the additional springs attached, which symmetric and antisymmetric bands are displayed separately. Here, $k_A = 10$ N/m and other parameters correspond to those in Fig. 2. As demonstrated, has no impact on antisymmetric bands because the distance between the lower-layer nanobeam and upper-layer nanobeam keeps constant as shown in Figs. 3(a), (c) and (e). But while adding more springs can constrain the symmetric vibration mode if the lower-layer and

$$\left(\begin{bmatrix} a[MG]+a[NG]+k_z[QG]+k_A[QG] & -k_z[PG]^T \\ -2k_z[PG] & 2k_z-2k_y(l-1) \end{bmatrix} - \omega^2 \begin{bmatrix} a[OG] & [0] \\ [0] & m_R \end{bmatrix}\right) \times \begin{bmatrix} [W_l(G)] \\ W_R(0) \end{bmatrix} = [0]. \quad (21)$$

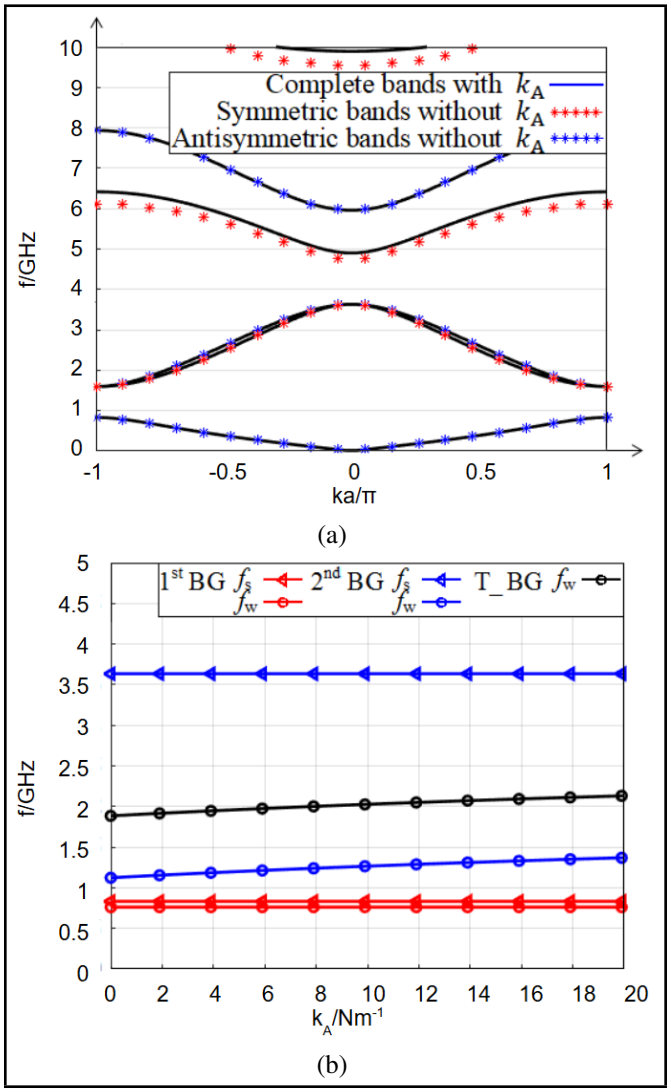

Figure 6. (a) Band structures of LR TMM PC double-layer nanobeams with and without attaching additional springs k_A, and (b) influences of k_A on starting frequencies f_s, widths f_w and total width of first two band gaps.

upper-layer nanobeams vibrate in different directions, the symmetric bands—aside from the first—can be effectively shifted upwards to higher frequency regions. Because the first symmetric band and second antisymmetric band almost coincide, the influence of k_A on such a band is not obvious. Figure 6 (b) shows the effects of on the beginning frequencies f_s, widths f_w, and overall width of the first two band gaps. Here, k_A changes from 0 N/m to 20 N/m. f_s and f_w of first band gap remains unaltered by increasing k_A since, as shown in Fig. 6 (a), the beginning and terminating frequencies are situated near the antisymmetric bands. Since the second band gap is settled in the antisymmetric band, its f_s likewise remains constant when k_A increases. However, because the ending frequency is situated at the symmetric band, the second band gap's f_w increases as k_A increases. Consequently, the total width keeps increasing same to the second bandgap width.

Figure 7 (a) depicts the band structure of the LR TMM PC double-layer nanobeam with the attached horizontal springs $k_y = 1$ N/m and $l = 2$. As a comparison, Fig. 7 (a) also gives the symmetric and antisymmetric bands without attaching horizontal springs. All the other parameters are corresponded to those in Fig. 2. Horizontal springs have no effect on symmetric bands since the masses remain static in this type of vibration mode, which makes it clear. Besides, the influences of k_y on other antisymmetric bands except for the first can be ignored. The first antisymmetric band descends to the lower frequency range because the primordial stiffness of k_z can be reduced by adding pre-compressed horizontal springs. The influences of k_y and l on starting frequencies f_s, widths f_w and total width of first two band gaps are displayed in Figs. 7 (b) and (c), separately. k_y is from 0 N/m to 2 N/m and l is from 1 to 3. The change of k_y and l can only affect the f_s of first band gap. The first band gap's f_s and f_w increase and decrease with an increase in k_y and l, respectively, which is consistent with Fig. 7 (a). Furthermore, as illustrated in Fig. 7(d), the impact of the coupling between k_y and l on f_w of the first band gap is also provided. The ranges of k_y and l are same to Figs. 7 (b) and (c). As shown, the larger value of k_y and l can obtain the larger pre-compression degree and lower equivalent stiffness, then the first band gap can be more easily opened.

Figure 8 illustrates the equivalent band structure when LR TMM PC double-layer nanobeam is equipped with additional springs and a horizontal spring. Except for $k_A = 10$ N/m, $k_y = 1$ N/m and $l = 2$, all the parameters are the same as those in Fig. 2. By comparing Fig. 8 with Fig. 2, the total width is increased from 3.5 GHz to 4.17 GHz and the opening rate is increased from to . Consequently, by regulating the symmetric and antisymmetric bands, the addition of horizontal and extra springs actively contributes to the opening of greater band gaps.

4. CONCLUSIONS

This article calculates the band structure of a double-layer nanobeam with surface effects, known as LR TMM PC. Moreover, band gap formation methods and regulation guidelines are disclosed. Main conclusions are followed:

1. Three complete band gaps under 10 GHz are identified, with symmetric and antisymmetric bands constituting the structure. Vibration is easily transmitted in the upper layer but can be suppressed in the lower layer within band gaps. Wider band gaps are achievable when excitation and response are on opposite sides.

2. To regulate these bands, additional and horizontal springs are strategically added. Increased stiffness in these springs widens the band gaps and raises their terminal frequencies. This unique regulation mechanism is exclusive to double-layer nanobeams.

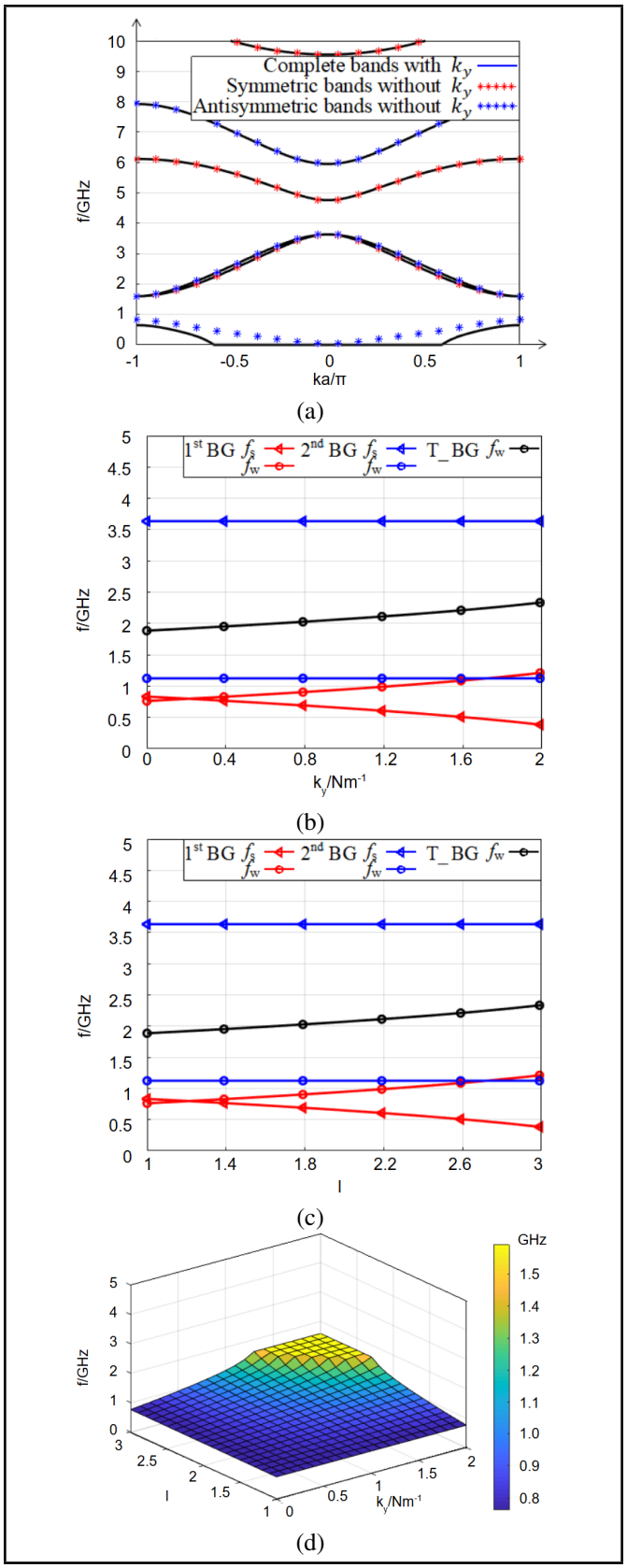

Figure 7. Band structures of LR TMM PC double-layer nanobeams with and without attaching horizontal springs k_y, influences of (b) k_y and (c) l on starting frequencies f_s, widths f_w and total width of first two band gaps, and (d) influence of the coupling between k_y and l on f_w of first band gap.

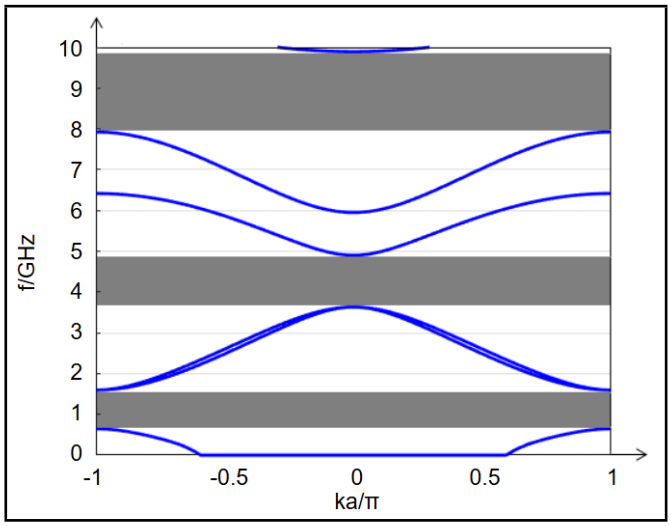

Figure 8. Band structure of LR TMM PC double-layer nanobeam with $k_A = 1$ N/m, $k_y = 1$ N/m and $l = 2$.

ACKNOWLEDGEMENTS

This research was supported by the National Natural Science Foundation of China (No. 52301373), the Young Elite Scientists Sponsorship Program by CAST (2022QNRC001) and the Natural Science Foundation of Jiangsu Higher Education Institutions of China (No. 22KJB580005).

REFERENCES

[1] Zhang S. Z., Hu Q. Q. and Zhao W. J., Surface effect on band structure of magneto-elastic phononic crystal nanoplates subject to magnetic and stress loadings, *Applied Mathematics and Mechanics(English Edition)*, **43**(2), 203-218, (2022). https://doi.org/10.1007/s10483-022-2806-7

[2] Liu X. H., Chen N., Jiao J. R. et al., Pneumatic soft phononic crystals with tunable band gap, *International Journal of Mechanical Sciences*, **240**, 107906, (2023). https://doi.org/10.1016/j.ijmecsci.2022.107906

[3] Hu Q. Q., Yang W. W. and Zhang S. Z., Studies on band structure of magneto-elastic phononic crystal nanoplates using the nonlocal theory, *Physics Letters A*, **423**, 127820, (2022). https://doi.org/10.1016/j.physleta.2021.127820

[4] Qian D. H., Wave propagation in a thermo-magneto-mechanical phononic crystal nanobeam with surface effects, *Journal of Materials Science*, **54**(6), 4766-4779, (2019). https://doi.org/10.1007/s10853-018-03208-7

[5] Qian D. H., Zhou P., Zhang J. et al., Tunability of resonator with pre-compressed springs on thermo-magneto-mechanical coupling band gaps of locally resonant phononic crystal nanobeam with surface effects, *Mechanical Systems and Signal Processing*, **176**, 109184, (2022). https://doi.org/10.1016/j.ymssp.2022.109184

[6] Ding R., Su X. L., Zhang J. J. et al., Tunability of longitudinal wave band gaps in one dimensional phononic crystal

with magnetostrictive material, *Journal of Applied Physics*, **115**, 074104, (2014). https://doi.org/10.1063/1.4866364

[7] Zhang S. Z. and Gao Y. W., Tunability of hysteresis-dependent band gaps in a two-dimensional magneto-elastic phononic crystal using magnetic and stress loadings, *Applied Physics Express*, **12**(2), 027001, (2019). https://doi.org/10.7567/1882-0786/aafa02

[8] Jin L. S. and Li L. J., Nonlinear Dynamics of Silicon Nanowire Resonator Considering Nonlocal Effect, *Nanoscale Research Letters*, **12**, 331, (2017). https://doi.org/10.1186/s11671-017-2106-9

[9] Qian D. H. and Wang J. C., Studies of a new-style resonator to control electro-mechanical coupling bandgap of a locally resonant piezoelectric/elastic phononic crystal double-layer nonlocal nanobeam, *Applied Mathematical Modelling*, **102**, 786-796, (2022). https://doi.org/10.1016/j.apm.2021.10.020

[10] He F. Y. and Qian D. H., Wave propagation in a non-local piezoelectric phononic crystal Timoshenko nanobeam, *Modern Physics Letters B*, **35**(3), 2150064, (2021). https://doi.org/10.1142/S0217984921500640

[11] Qian D. H., Wu J. H. and He F. Y., Electro-mechanical coupling band gaps of a piezoelectric phononic crystal Timoshenko nanobeam with surface effects, *Ultrasonics*, **109**, 106225, (2021). https://doi.org/10.1016/j.ultras.2020.106225

[12] Zhou Y., Xu Y., Pan D. et al., Improved incorporation of strain gradient elasticity in the flexoelectricity based energy harvesting from nanobeams, *Physica E: Low-dimensional Systems and Nanostructures*, **98**, 148-158, (2018). https://doi.org/10.1016/j.physe.2017.12.037

[13] Zeng S., Wang B. L. and Wang K. F., Static stability analysis of nanoscale piezoelectric shells with flexoelectric effect based on couple stress theory, *Microsystem Technologies*, **24**(7), 2957-2967, (2018). https://doi.org/10.1007/s00542-018-3734-4

[14] Zhang S. Z. and Gao Y. W., Surface effect on band structure of flexural wave propagating in magneto-elastic phononic crystal nanobeam, *Journal of Physics D: Applied Physics*, **50**(44), 445303, (2017). https://doi.org/10.1088/1361-6463/aa8878

[15] Cao D. X., Hu W. H., Gao Y. H. et al., Vibration and energy harvesting performance of a piezoelectric phononic crystal beam, *Smart Materials and Structures*, **28**(8), 085014, (2017). https://doi.org/10.1088/1361-665X/ab2829

[16] Lee H., Oh J. H. and Kim Y. Y., Multiple beam splitting in elastic phononic crystal plates, *Ultrasonics*, **56**, 178-182, (2015). https://doi.org/10.1016/j.ultras.2014.10.012

[17] Deng T., Zhang S. Z. and Gao Y. W., A magnetic-dependent vibration energy harvester based on the tunable point defect in 2D magneto-elastic phononic crystals, *Crystals*, **9**(5), 261, (2019). https://doi.org/10.3390/cryst9050261

[18] Sun W. B., Wang T., Sun X. W. et al., Defect states and vibration energy recovery of novel two-dimensional piezoelectric PC plate, *Acta Physica Sinica*, **68**(23), 234206, (2019). https://doi.org/10.7498/aps.68.20190260

[19] Guo X., Wei P., Lan M. et al., Dispersion relations of elastic waves in one-dimensional piezoelectric/piezomagnetic phononic crystal with functionally graded interlayers, *Ultrasonics*, **70**, 158-171, (2016). https://doi.org/10.1016/j.ultras.2016.04.025

[20] Zhu J., Hu P. Y., Chen Y. D. et al., Waves Propagating in Nano-Layered Phononic Crystals with Flexoelectricity, Microstructure, and Micro-Inertia Effects, *Nanomaterials*, **12**(7), 1080, (2022). https://doi.org/10.3390/nano12071080

[21] Li C., Liu M. and Song M. T., Modeling and Analysis of Elastic Waves in One-Dimensional Micro-Nano Phononic Crystals Based on the Nonlocal Theory, *Journal of Vibration Engineering & Technologies*, **10**(4), 1265-1278, (2022). https://doi.org/10.1007/s42417-022-00442-x

[22] Liu Y., Xu A. and Ning R., Study of temperature and mechanical properties and constitutive equation for modified BMI/DPA and CTBN toughened epoxy, *Journal of Aeronautical Materials*, **3**(1), 44-51, (1999). https://doi.org/1005-5053(1999)04-0044-08

[23] Aharoni A., Demagnetizing factors for rectangular ferromagnetic prisms, *Journal of Applied Physics*, **83**(6), 3432-3434, (1998). https://doi.org/10.1063/1.3536518

[24] Ding R., Su X., Zhang J. et al., Tunability of longitudinal wave band gaps in one dimensional phononic crystal with magnetostrictive material, *Journal of Applied Physics*, **115**(7), 2022-364, (2014). https://doi.org/10.1063/1.4866364

APPENDIX

This appendix gives the solution procedure of elastic coefficient c_{11}, piezomagnetic coefficient q_{11} and magnetic permeability μ_{11} of magnetostrictive material Terfenol-D in detail.

If the demagnetization effect is considered, the non-linear TMM coupling constitutive equations are written as:[12]

$$\begin{cases} \epsilon_x = \frac{\sigma_x}{E_s} + \alpha\Delta T - \frac{\beta\Delta T M_x^2}{M_s^2} \\ \quad + \begin{cases} \lambda_s \tanh(\frac{\sigma_x}{\sigma_s}) + [1-\tanh(\frac{\sigma_x}{\sigma_s})]\frac{\lambda_s}{M_s^2} M_x^2 \frac{\sigma_x}{\sigma_s} \geq 0 \\ \frac{\lambda_s}{2}\tanh(\frac{2\sigma_x}{\sigma_s}) + [1-\frac{1}{2}\tanh(\frac{2\sigma_x}{\sigma_s})]\frac{\lambda_s}{M_s^2} M_x^2 \frac{\sigma_x}{\sigma_s} < 0 \end{cases} \\ H_x - \eta M_x = \frac{1}{k} f^{-1}(\frac{M_x}{M_s^T}) + \frac{2\beta\Delta T \sigma_x M_x}{\mu_0 M_s^2} \\ \quad - \begin{cases} 2\{\sigma_x - \sigma_s \ln[\cosh(\frac{\sigma_x}{\sigma_s})]\}\frac{\lambda_s}{\mu_0 M_s^2} M_x \frac{\sigma_x}{\sigma_s} \geq 0 \\ 2\{\sigma_x - \frac{\sigma_s}{4}\ln[\cosh(\frac{2\sigma_x}{\sigma_s})]\}\frac{\lambda_s}{\mu_0 M_s^2} M_x \frac{\sigma_x}{\sigma_s} < 0 \end{cases} \end{cases} ; \tag{A.1}$$

Here, ϵ_x is the strain in x-direction and M_x is the magnetization intensity in x-direction. $\Delta T = T - 0°C$, $M_s^T = M_s(1 - \frac{T+273}{T_c+273})^{1/2}/(\frac{T_c}{T_c+273})^{1/2}$, α is the thermal expansion constant, $k = 3\chi_m/M_s^T$ is the relaxation factor, $f(x) = \coth(x) - 1/x$ is the non-linear Langevin function, and η is the demagnetization factor.

η can be expressed as:[21]

$$\begin{aligned} \pi\eta = (p - \frac{1}{p})\ln(\frac{\sqrt{p^2+2}+1}{\sqrt{p^2+2}-1}) + \frac{2}{p}\ln(\sqrt{2}+1) + p\ln(\frac{\sqrt{p^2+2}-1}{\sqrt{p^2+2}+1}) \\ 2\arctan(\frac{1}{p\sqrt{p^2+2}}) + \frac{2(1-p^2)}{3p}\sqrt{p^2+2} + \frac{2(1-p^3)}{3p} - \frac{2^{\frac{3}{2}}}{3p} \\ + \frac{2}{3}\sqrt{p^2+1}(2p - \frac{1}{p}); \end{aligned} \tag{A.2}$$

where $p = a_1/b$.

Eq. (A.1) can be rewritten as equivalent linear-like constitutive equations:[22]

$$\begin{cases} \sigma_x = c_{11}(\sigma_x, H_x, \Delta T)\epsilon_x - q_{11}(\sigma_x, H_x, \Delta T)H_x + \alpha_{11}(\sigma_x, H_x, \Delta T)\Delta T \\ B = c_{11}(\sigma_x, H_x, \Delta T)\epsilon_x - \mu_{11}(\sigma_x, H_x, \Delta T)H_x + p_{11}(\sigma_x, H_x, \Delta T)\Delta T \end{cases} ; \tag{A.3}$$

where B_x is the magnetic induction field in x-direction, α_{11} is the thermal expansion coefficient and p_{11} is the heat transfer coefficient. The coefficients c_{11}, q_{11} and μ_{11} can be expressed:[22]

$$\begin{cases} c_{11}(\sigma_x, H_x, \Delta T) = 1/(\frac{\delta\epsilon_x(\sigma_x, H_x, \Delta T)}{\delta\sigma_x}) \\ q_{11}(\sigma_x, H_x, \Delta T) = \frac{\delta\epsilon_x(\sigma_x, H_x, \Delta T)}{\delta\sigma_x} c_{11} \\ \mu_{11}(\sigma_x, H_x, \Delta T) = \mu_0(1 + \frac{M_x}{H_x}) - (\frac{\delta\epsilon_x(\sigma_x, H_x, \Delta T)}{\delta\sigma_x})^2/(\frac{\delta\epsilon_x(\sigma_x, H_x, \Delta T)}{\delta\sigma_x}) \end{cases} . \tag{A.4}$$

Define:

$$\frac{M_x}{M_S^T} = \begin{cases} \coth M_1 - \frac{1}{M_1}\frac{\sigma_x}{\sigma_s} \geq 0 \\ \coth M_2 - \frac{1}{M_2}\frac{\sigma_x}{\sigma_s} < 0 \end{cases} ; \tag{A.5}$$

where

$$\begin{bmatrix} M1 \\ M2 \end{bmatrix} = k(H_x - \eta M_x) - \frac{2k\beta\Delta T\sigma_x M_x}{\mu_0 M_s^2} + \begin{cases} 2\{\sigma_x - \sigma_s \ln[\cosh(\frac{\sigma_x}{\sigma_s})]\}\frac{\lambda_s}{\mu_0 M_s^2} M_x \frac{\sigma_x}{\sigma_s} \geq 0 \\ 2\{\sigma_x - \frac{\sigma_s}{4}\ln[\cosh(\frac{2\sigma_x}{\sigma_s})]\}\frac{\lambda_s}{\mu_0 M_s^2} M_x \frac{\sigma_x}{\sigma_s} < 0 \end{cases} ; \tag{A.6}$$

Combining Eqs. (A.1), (A.5) and (A.6), it can be obtained:

$$\begin{cases} \frac{\delta\epsilon_x(\sigma_x, H_x, \Delta T)}{\delta\sigma_x} = \frac{1}{E_s} - \frac{2\beta\Delta T M_x}{M_s^2}\frac{\delta M_x}{\delta\sigma_x} \\ \quad + \begin{cases} \frac{\lambda_s}{\sigma_s}\operatorname{sech}^2\frac{\sigma_x}{\sigma_s}(1 - \frac{M_x^2}{M_s^2}) + \frac{2\lambda_s}{M_s^2}[1 - \tanh\frac{\sigma_x}{\sigma_s}]M_x\frac{\delta M_x}{\delta\sigma_x} & \frac{\sigma_x}{\sigma_s} \geq 0 \\ \frac{\lambda_s}{\sigma_s}\operatorname{sech}^2\frac{2\sigma_x}{\sigma_s}(1 - \frac{M_x^2}{M_s^2}) + \frac{2\lambda_s}{M_s^2}[1 - \frac{1}{2}\tanh\frac{2\sigma_x}{\sigma_s}]M_x\frac{\delta M_x}{\delta\sigma_x} & \frac{\sigma_x}{\sigma_s} < 0 \end{cases} \\ \frac{\delta\epsilon_x(\sigma_x, H_x, \Delta T)}{\delta H_x} = -\frac{2\beta\Delta T M_x}{M_s^2}\frac{\delta M_x}{\delta H_x} \\ \quad + \begin{cases} [1 - \tanh\frac{\sigma_x}{\sigma_s}]\frac{2\lambda_s M_x}{M_s^2}\frac{\delta M_x}{\delta H_x} & \frac{\sigma_x}{\sigma_s} \geq 0 \\ [1 - \frac{1}{2}\tanh\frac{2\sigma_x}{\sigma_s}]\frac{2\lambda_s M_x}{M_s^2}\frac{\delta M_x}{\delta H_x} & \frac{\sigma_x}{\sigma_s} < 0 \end{cases} \end{cases} ; \tag{A.7}$$

where

$$\begin{cases} \dfrac{\delta M_x}{\delta \sigma_x} = \begin{cases} \dfrac{2k\lambda_s[1-\tanh(\frac{\sigma_x}{\sigma_s})]M_x - 2k\beta\Delta T M_x}{\frac{\mu_0 M_s^2}{M_s^T(-\operatorname{csch}^2 M_1 + M_1^{-2})} - 2k\lambda_s\{\sigma_x - \sigma_s \ln[\cosh(\frac{\sigma_x}{\sigma_s})]\} + k\eta\mu_0 M_s^2 + 2k\beta\Delta T\sigma_x} \\ \dfrac{2k\lambda_s[1-\frac{1}{2}\tanh(\frac{2\sigma_x}{\sigma_s})]M_x - 2k\beta\Delta T M_x}{\frac{\mu_0 M_s^2}{M_s^T(-\operatorname{csch}^2 M_2 + M_2^{-2})} - 2k\lambda_s\{\sigma_x - \frac{\sigma_s}{4}\ln[\cosh(\frac{2\sigma_x}{\sigma_s})]\} + k\eta\mu_0 M_s^2 + 2k\beta\Delta T\sigma_x} \end{cases} \\ \dfrac{\delta M_x}{\delta H_x} = \begin{cases} \dfrac{k\mu_0 M_s^2}{\frac{\mu_0 M_s^2}{M_s^T(-\operatorname{csch}^2 M_1 + M_1^{-2})} - 2k\lambda_s\{\sigma_x - \sigma_s \ln[\cosh(\frac{\sigma_x}{\sigma_s})]\} + k\eta\mu_0 M_s^2 + 2k\beta\Delta T\sigma_x} \\ \dfrac{k\mu_0 M_s^2}{\frac{\mu_0 M_s^2}{M_s^T(-\operatorname{csch}^2 M_2 + M_2^{-2})} - 2k\lambda_s\{\sigma_x - \frac{\sigma_s}{4}\ln[\cosh(\frac{2\sigma_x}{\sigma_s})]\} + k\eta\mu_0 M_s^2 + 2k\beta\Delta T\sigma_x} \end{cases} \end{cases} . \tag{A.8}$$

By substituting Eq. (A.7) into Eq. (A.4), c_{11}, q_{11} and μ_{11} can be finally obtained.